Main Manuscript for

Electrical control of the transduction channels' gating force in mechanosensory hair cells.

SHORT TITLE: Control of the channel-gating force in hair cells

Achille Joliot[1,2], Laure Stickel[1,2] and Pascal Martin[1,2,*]

[1] Physique des Cellules et Cancer, Institut Curie, PSL Research University, CNRS UMR168, F-75248 Paris, France.

[2] Sorbonne Université, F-75252 Paris, France.

[*] Correspondence: pascal.martin@curie.fr

Keywords: auditory system, bioelectricity, gating compliance, mechanosensitive ion channels, vestibular system.

The main manuscript includes:

Main Text

Figures 1 to 6

ABSTRACT

The inner ear's hair cells rely on mechanosensitive ion channels to convert vibrations of their hair bundles into electrical signals. The mechanical correlates of channel gating—the gating force and the gating swing—are fundamental determinants of hair-cell mechanosensitivity but are still poorly understood. Here we show that varying the electrical potential across the sensory hair-cell epithelium continuously modulates the gating force, by up to $\pm 100\%$. Our observations also revealed an abrupt transition between states of weak and strong gating force at a threshold potential, so that strong gating forces associated to high mechanosensitivity are observed only when the calcium influx through the channels is large enough, but not too large. Gating-force changes, remarkably enough, were explained by the modularity of the gating swing, ranging from values comparable to the channel pore size to nearly tenfold larger. Gating-swing control is expected to underly the hair cell's ability to tune its mechanosensitivity to minute sound stimuli.

TEASER: Mechanosensitivity of ion-channel gating in hair cells can be tuned by the electrical potential across the sensory epithelium.

INTRODUCTION

Mechanoreception by the inner ear's sensory hair cells begins with the deflection of their hair bundle—a cohesive tuft of cylindrical stereocilia arranged in a staircase pattern (1–3). A deflection toward the taller row of stereocilia increases mechanical tension in oblique tip links, which connect the tip of each stereocilium to the flank of a taller neighbor. The increased tip-link tension opens mechanosensitive ion channels and evokes an influx of cations into the hair cell, primarily K^+ ions but also Ca^{2+} ions.

Our understanding of hair-cell mechanosensitivity is informed by the gating-spring model of mechanoelectrical transduction (4, 5). Within this framework, the transduction channels are gated directly by force, which is transmitted to the channels via elastic elements—the gating springs—that operate in series with the tip links. The product of the gating-spring stiffness and the gating swing defines the gating force, a fundamental determinant of hair-cell mechanosensitivity: its magnitude sets the maximal slope of the sigmoidal relation between the transduction current and the deflection of the hair bundle (fig. S1, A and B). The greater the gating force, the larger the transduction current evoked by a small stimulus, making the hair cell more sensitive to a given deflection of its hair bundle.

The gating-spring model imposes a reciprocal relationship between tip-link tension and channel gating. If tensioning the tip links evokes channel opening, then channel opening must reduce tip-link tension by an amount given precisely by the gating force. Feedback between tip-link tension and channel gating produces gating compliance, the effective softening of the hair bundle upon channel gating (6, 7). For large positive or negative bundle displacements, at which the transduction channels are nearly all open or closed, respectively, the force-displacement relation is linear. At intermediate displacements that elicit channel gating, however, the slope of the force-displacement relation is reduced: the hair bundle is effectively softer. Gating compliance is associated with a shift between the two linear limbs of the force-displacement relation; this shift provides an estimate of the combined gating force, denoted F_G in the following, produced by the ensemble of transduction channels that operate in parallel within the hair bundle (fig. S1B). Furthermore, upon an oscillatory movement of the hair bundle, opening and closing of the transduction channels also increase friction on the hair bundle, a phenomenon called gating friction (8). The experimental demonstration of gating compliance and gating friction at the cellular scale of a micron-sized hair bundle provides strong support for the gating-spring model. Because these phenomena reflect the mechanical correlate of

channel gating, they can also be used to infer fundamental properties of channel gating at the molecular scale such as the gating force (6, 7, 9).

Biophysical estimates of the gating force are variable, even with hair cells from the same animal species and organ. With hair cells in excised preparations of the mammalian cochlea, there is some evidence of gating compliance (10–12) but gating forces can also be so weak that the force-displacement relation remains linear (13, 14). In these experiments, however, the endocochlear potential that normally boosts transduction currents in vivo is absent and the hair cells are fully immersed in a standard extracellular fluid called perilymph. This condition disrupts the two ionic compartments that hair cells experience in vivo, with endolymph and perilymph bathing the cells' apical and basal aspects, respectively. In the frog saccule, gating forces can lead to a moderate (about 40%) decrease in hair-bundle stiffness (6) or be strong enough to result in negative stiffness, which can lead to spontaneous oscillations of the hair bundle and, in turn, frequency-selective amplification of periodic stimuli (9, 15–17). Remarkably enough, strong gating forces and negative stiffness were reported only under ex-vivo conditions that closely mimic natural ones, with reconstituted endolymph-perilymph compartments.

The reason for the apparent variability of the gating force is unclear. Variability may result from hair-cell damage inflicted by artificial ex-vivo conditions or instead reflect an intrinsic ability of the hair cell to control the magnitude of its gating force under variable conditions. These observations call for a comprehensive and systematic investigation of the gating force under a range of physiological conditions.

In this work, we report that the electrical potential across the sensory epithelium that houses the hair cells can serve as a control parameter of the gating force. Our results indicate that the gating force varies primarily because the gating swing varies. Our work further reveals a reversible, but hysteretic, transition between a state of strong gating force, for which the hair bundles oscillate spontaneously, and a state of weak gating force, for which hair-bundle mechanics is linear and the hair bundles are quiescent. We finally provide evidence that these effects are mediated, at least in part, by electrical control of the influx of Ca^{2+} through the transduction channels.

RESULTS

We took advantage of an excised preparation of the frog saccule that mimics *ex vivo* the two-compartment ionic conditions that the sensory epithelium experiences *in vivo*. Under these conditions, the hair cells routinely displayed spontaneous oscillations of their hair bundles, as recognized before (18–20). We aimed here at evaluating the effects of a transepithelial potential on hair-bundle mechanics. To this end, we used a pair of electrodes and a current generator to impose a transepithelial current, I, within a range of ± 10 μA (fig. S2A). Upon application of a current step, the transepithelial potential, U, reached a steady-state value in about 600 μs (fig. S2B). As a rule of thumb, a positive current of $+1$ μA evoked a positive potential in the endolymphatic compartment of $+10$ mV with respect to the perilymphatic compartment; accordingly, the transepithelial potential thus varied within a range of ± 100 mV. We emphasize for the following that a positive endolymphatic potential is expected to increase the influx of K^+ and Ca^{2+} ions through the transduction channels, whereas a negative potential does the opposite. All numerical results are given below as the average and standard deviations (SD) over an ensemble of n independent measurements.

The potential modulates strongly the gating force but weakly the hair-bundle stiffness

To determine the effects of an endolymphatic potential on the mechanical properties of a hair bundle, we measured the bundle's force-displacement relation in response to a series of step displacements applied to the base of a stimulus fiber (Fig. 1). Under control conditions, for which no transepithelial current was applied ($I = 0$), the force-displacement relation showed a prominent region of reduced slope, or gating compliance, which is expected for hair bundles that oscillate spontaneously (9, 16). A fit of the relation to Equation 1 (Methods) yielded a set-point deflection $X_0 = -2 \pm 7$ nm, a gating force $F_G = 17 \pm 4$ pN and a linear stiffness $K = 0.85 \pm 0.2\ \mathrm{pN \cdot nm^{-1}}$ (mean ± SD; $n = 29$ in 16 frogs). We recall that the set-point deflection can be interpreted as the deflection that leads to a channels' open probability of ½ (16). For each hair bundle, the procedure was repeated in the presence of a static transepithelial current ($I \neq 0$).

We start by presenting the effects of a transepithelial current on a force-displacement relation in four representative examples (Fig. 1); the effects on the corresponding spontaneous hair-bundle oscillations are shown in Supplementary Materials (fig. S3, A to D). Applying a positive current, here $I = +3$ μA, corresponding to a positive endolymphatic potential $U \simeq +30$ mV,

evoked an increase of the set-point deflection: the transduction channels closed (Fig. 1A). In addition, we observed a small (-5%) decrease of the linear bundle's stiffness and, remarkably, a large decrease (-38%) of the gating force. In another cell, a larger current $I = +6$ μA resulted in a similar change in stiffness (-6%) but evoked a larger decrease of the gating force (-50%; Fig. 1B). Conversely, applying a negative current of moderate magnitude, here $I = -3$ μA, corresponding to a negative endolymphatic potential $\mathrm{U} \simeq -30$ mV, elicited a decrease of the set-point deflection and thus opening of the transduction channels, a small increase ($+10\%$) of the linear stiffness, and a large increase ($+89\%$) of the gating force (Fig. 1C). Furthermore, applying a large transepithelial current, here $\mathrm{I} = -6$ μA, led to an unexpected finding: the force-displacement relation became linear (Fig. 1D). This is not because the integrity of the hair cell was impaired by application of a large transepithelial current, for all the effects were fully reversible.

Performing an ensemble of $n = 41$ pairs of measurements in 29 hair bundles from 16 frogs confirmed the effects illustrated by the four representative examples. We found a strong positive correlation between the change, $\Delta X_0 = X_0(I) - X_0(I = 0)$, of the set-point deflection and the applied transepithelial current (Fig. 2A). This correlation came as no surprise: the endolymphatic potential resulting from the transepithelial current should influence the magnitude of the Ca^{2+} influx through the transduction channels and calcium is known to promote channel closure (4, 16, 21–23). The change in linear stiffness, $\Delta K = K(I) - K(I = 0)$, was negatively correlated to the transepithelial current, but only weakly (Fig. 2B). Instead, for currents $I > -4$ μA, the change, $\Delta F_G = F_G(I) - F_G(I = 0)$, of the hair-bundle's gating force displayed a strong negative correlation with the current (Fig. 2C). The relative variation of the gating force was correspondingly much larger than that of the linear stiffness (Fig. 2D). A positive transepithelial current evoked a reduction of the gating force by as much as -80%, whereas the stiffness decreased at most by -10% over the same range of transepithelial currents. Conversely, the gating force could nearly double in the presence of a negative transepithelial current, corresponding to a relative increase of $+100\%$, whereas stiffness did not increase beyond $+25\%$. These correlations between mechanical properties of the hair bundle and the transepithelial current were associated to systematic changes of the frequency, amplitude and waveform of spontaneous hair-bundle oscillations (fig. S3, E to G).

For all the seven hair bundles for which the transepithelial current was more negative than -5 μA, corresponding to an endolymphatic potential $U \leq -50$ mV, the gating force did not

follow the trend observed at more positive potentials. Instead of increasing further or saturating at more negative potentials, the gating force dropped to values so low that the force-displacement relation was linear, thus with no detectable signature of gating compliance (Figs. 1D and 2, C and D). At these endolymphatic potentials, no spontaneous oscillation was observed; the hair bundles were quiescent (fig. S3D). Our study thus revealed the existence of a critical value of the transepithelial current, $I = I_C \simeq -5\ \mu A$, and of the endolymphatic potential, $U = U_C \simeq -50$ mV, that delimited two functional states of the hair bundle: a state of strong gating force for which gating compliance was large enough to yield spontaneous oscillations of the hair bundle and a state of weak gating force for which hair-bundle mechanics was linear and the hair bundle was quiescent.

The gating force varies because the gating swing varies

Within the framework of the gating-spring model (fig. S1A)**,** the gating force for the whole hair bundle, $F_G = K_{GS}D$, is the product of the combined stiffness of the gating springs, K_{GS}, and of the gating swing, D, of a transduction channel. Remarkably enough, the relative effect of an endolymphatic potential on the gating force was much larger than that on the hair-bundle stiffness (Fig. 2D): the gating force could vary by as much as about $\pm 100\%$, whereas stiffness in the same hair bundles varied only from -10% to $+25\%$. Because the gating springs are expected to contribute a significant fraction of the total hair-bundle stiffness (24), K, we reasoned that the change in gating force resulted mainly from a change in the magnitude of the gating swing. We could confirm this inference by measuring the hair-bundle stiffness, $K_{SP} = 0.17 \pm 0.03\ \mathrm{pN \cdot nm^{-1}}\ (n = 14)\ \simeq 0.2\ K$, after disruption of the tip links. By subtracting the average value of K_{SP} to individual measurements of K, we could then estimate, for each hair bundle, the gating-spring stiffness $K_{GS} = K - K_{SP}$, and in turn the gating swing D. After projection along the oblique axis of the tip links using the projection factor $\gamma = 0.14$ (25), we found a gating swing $d = \gamma D = 3.7 \pm 1.4$ nm $(n = 29)$ under control conditions (Fig. 3A). Replicating the behavior of the gating force, the gating-swing change displayed a strong negative correlation with the transepithelial current for currents $I \geq I_C \simeq -5\ \mu A$ (Pearson correlation $r = -0.86$; p-value $= 1 \cdot 10^{-10}$) and dropped to undetectable levels for $I \leq I_C$. For $I \geq I_C$, the gating swing d could reach a value of up to about 8 nm in the presence of a negative endolymphatic potential or, conversely, be as small as 2 nm upon application of a potential of opposite polarity (Fig. 3B).

192 **The transition between states of strong and weak gating force shows hysteresis**

193 To further explore the transition between states of strong and weak gating force (Figs. 1D and
194 2C), we applied ramps of transepithelial current (Fig. 4A) while the hair bundle was subjected
195 to triangular mechanical stimulation (Fig. 4B). This stimulation protocol allowed to monitor,
196 continuously for the same hair bundle, how the mechanical properties varied as a function of
197 the transepithelial current. The ramps were slow enough that the transepithelial current varied
198 by only ~0.2 μA over the time required to measure a force-displacement cycle (see Methods).
199 Because this variation was too small to elicit a significant variation of the gating force (Fig. 2D),
200 the mechanical measurements were quasi static. The mechanical stimulus elicited a force-
201 displacement cycle with clockwise circulation, corresponding to energy dissipation (8). The
202 cycle displayed a region of lower slope—gating compliance—on the positive and negative half
203 cycles (Fig. 4C), where the channels opened and closed, respectively. In addition, the height of
204 the force-displacement cycle was larger within the region of channel gating. This property was
205 previously shown to result from the contribution of the transduction channels' gating force to
206 hair-bundle friction, a phenomenon called gating friction, and the displacement at which the
207 cycle had a maximal height (abscissa of disks in Fig. 4C) was identified as the set-point
208 deflection X_0 (8). In the following, the maximal half-height of the cycle, ϕ_{MAX}, was used as a
209 reporter for the magnitude of the gating force.

210 As the transepithelial current decreased from zero to negative values, the region of gating
211 compliance and gating friction in the force-displacement cycle shifted toward more negative
212 displacements, corresponding to a decrease of the set-point deflection and thus opening of the
213 transduction channels (Fig. 4C, movie S1). Following the point of inversion symmetry in a
214 force-displacement cycle resulted in a nearly linear trajectory of slope $0.4 \pm 0.2\ \mathrm{pN \cdot nm^{-1}}$
215 ($n = 8$; Fig. 4D). In addition, the height of the force-displacement cycle, and thus the maximal
216 friction force ϕ_{MAX} increased before saturating (Fig. 4E). When the absolute magnitude of the
217 negative current became large enough, corresponding to $I \leq I_C = -3.7 \pm 1\ \mu\mathrm{A}$ and an
218 endolymphatic potential $U \leq U_C \simeq -37 \pm 10\ \mathrm{mV}$ ($n = 8$), the friction force ϕ_{MAX} dropped
219 (Fig. 4, E and F, and movie S1) until the nonlinearity vanished (Fig. 4C, red). These
220 observations on single hair cells (solid line in Fig. 4E) mirrored the measured changes of the
221 gating force upon application of a static transepithelial current in an ensemble of cells (Fig. 2C).
222 We note that gating friction generally depends on the activation time of the transduction
223 channels, not just on the gating force (8). Detailed analysis of the force-displacement cycles

suggests that the channel-activation time had increased by about 50%, on average, when the friction force ϕ_{MAX} reached a saturating value upon application of a negative transepithelial current (fig. S4). The observed variation of hair-bundle friction (Fig. 4, E and F) thus resulted from modulation of both the channel-activation time and the gating force (Fig. 2C).

The polarity of the current ramp was then reversed. As the negative current increased, the set-point deflection increased and the point of inversion symmetry in the force-displacement cycle showed a nearly linear trajectory of slope $0.6 \pm 0.2\ \mathrm{pN} \cdot \mathrm{nm}^{-1}$ ($n = 8$; Fig. 4, C and D). In addition, the signatures of gating compliance and gating friction, associated to nonlinear force-displacement relations, were retrieved. The nonlinearity, however, reappeared at a negative current with a smaller absolute value than that necessary to conceal the signatures of channel-gating forces on the descending ramp. Over an ensemble of $n = 8$ cells, we measured a shift in the transepithelial current of 2.3 ± 0.8 µA, corresponding to a 20-mV difference of endolymphatic potential. Thus, the transition between states of strong and weak gating force displayed hysteresis (Fig. 4E).

The transition kinetics between the two states occurs on a sub-second timescale

To characterize the kinetics of the transition between states of strong and weak gating force, we applied large negative steps of transepithelial current, here $I = -8$ µA (Fig. 5), while continuously measuring a hair bundle's force-displacement cycle in response to triangular mechanical stimulation. As expected from the effects of current ramps (Fig. 4), the force-displacement cycle shifted in the negative direction along the displacement axis and the force-displacement cycle lost the signatures of gating compliance and gating friction (Fig. 5A, movie S2). The time courses of the average hair-bundle position on the cycle, denoted $\bar{X}$ in the following, and of the maximal friction force ϕ_{MAX} were quantified by measuring the $10 - 90\%$ decay and rise times following the onset and offset of the current step, respectively. Over an ensemble of $n = 4$ hair cells, the characteristic time, $\tau_X^{ON} = 500 \pm 50$ ms, of negative hair-bundle motion evoked by the current step was fivefold longer than that, $\tau_X^{OFF} = 100 \pm 30$ ms, necessary to return to the initial position after the current was turned off (Fig. 5B). The friction force ϕ_{MAX} showed an opposite behavior: its decay time, $\tau_\Phi^{ON} = 180 \pm 40$ ms, after the onset of the current step was twofold shorter than its rise time, $\tau_\Phi^{OFF} = 400 \pm 100$ ms, during recovery (Fig. 5B). Note that the time required to measure a force-displacement cycle

was here of only 20 ms. This duration was about ten times shorter than $\tau_{\Phi}^{OFF/ON}$ and thus short enough to ensure a quasistatic assessment of hair-bundle mechanics (Methods).

There was thus a separation of timescales between the changes of $\bar{X}$ and ϕ_{MAX}. At the onset of the current step, gating compliance vanished before the negative shift had completed: $\tau_{\Phi}^{ON}/\tau_{X}^{ON} = 0.37 \pm 0.17$ (Fig. 5, B and C). In contrast, after the external transepithelial current was turned off, the mechanical nonlinearity recovered more slowly than the average position of the hair bundle: $\tau_{\Phi}^{OFF}/\tau_{X}^{OFF} = 4.2 \pm 2$ (Fig. 5, B and C).

Reducing the endolymphatic Ca^{2+} concentration replicates the effects of a negative endolymphatic potential

A negative endolymphatic potential may have mediated its effects on the gating force by reducing the magnitude of the Ca^{2+} influx through the transduction channels. To test this hypothesis, we used iontophoresis of a Ca^{2+} chelator to reduce the endolymphatic Ca^{2+} concentration near a hair bundle and, in turn, the Ca^{2+} influx through the channels. In response to descending and ascending ramps of iontophoretic current (Fig. 6A), or equivalently of Ca^{2+} concentration, we again observed an increase in hair-bundle friction followed by a reversible but hysteretic transition between states of strong and weak gating force (Fig. 6, B and C, and movie S3). Repeating the experiments over an ensemble of $n = 8$ cells confirmed the robustness of these effects (Fig. 6D) and how they mirrored those observed upon modulation of the endolymphatic potential (Fig. 4). In addition, the force-displacement relation of a hair bundle could show strong gating compliance under control conditions but reversibly become linear upon step application of a Ca^{2+} chelator, with no noticeable change in the linear stiffness of the hair bundle (Fig. 6E). The same behavior was observed in $n = 7$ hair cells. Thus, enough calcium in endolymph was required for the hair bundle to evince strong gating forces.

DISCUSSION

In this work, we showed that varying the endolymphatic potential modulates the gating force continuously and reversibly, thus serving as a control parameter for the mechanosensitivity of the hair cell to minute deflections of its hair bundle. This bioelectric effect is large; the gating force could nearly double upon application of negative potentials and, conversely, could be reduced by up to 80% of the control value at positive potentials (Fig. 2D). A major finding of our study is that the gating force varied because the gating swing varied, with only minor effects on the gating-spring stiffness (Figs. 2D and 3). In addition, our observations revealed an

285 unexpected transition between two functional states of the hair bundle—one with low
286 mechanosensitivity and one with high mechanosensitivity: a quiescent state of weak gating
287 force with gating swings of about one nanometer or less, and an oscillatory state of strong gating
288 force with gating swings up to ten times larger, respectively. The hair cell switched from a state
289 of strong gating force to a state of weak gating force when the endolymphatic potential became
290 more negative than a critical value $U = U_C \simeq -50$ mV (Figs. 1D, 2C, and 4, C and E). At such
291 negative potentials, the electromotive force driving the influx of cations through the
292 transduction channels is expected to be greatly reduced. Because reducing the Ca^{2+}
293 concentration near a hair bundle evoked a similar transition (Fig. 6), the strong gating forces
294 and large gating swings associated to high mechanosensitivity likely required a resting Ca^{2+}
295 influx through the transduction channels that was large enough. Altogether, our findings
296 demonstrate the modularity of the molecular determinants of hair-bundle mechanosensitivity—
297 specifically, the transduction channels' gating force and gating swing—in response to
298 variations in physiological control parameters.

299 **Physiological role of the endolymphatic potential**

300 Like other epithelia, the sensory epithelia that house the hair cells in the vertebrate inner ear are
301 polar tissues that experience a transepithelial potential under natural conditions (26). This
302 potential generally lies within a range $1 - 10$ mV, except in the mammalian cochlea where the
303 endolymphatic potential can reach $+100$ mV. Remarkably enough, this high value of the
304 endolymphatic potential is associated with a Ca^{2+} concentration in endolymph, about 20 μM,
305 which is about one of order of magnitude lower than in hearing organs from non-mammalian
306 species or than in vestibular organs. Our results on frog saccular hair cells (Figs. 2 and 6)
307 suggest that the combination of a large endolymphatic potential and a low Ca^{2+} concentration
308 in the cochlea might maintain a Ca^{2+} influx within the optimal range to allow for large gating
309 forces while boosting the magnitude of transduction currents. In support of this inference, a
310 mechanical nonlinearity attributed to hair-bundle mechanics has been measured in an ex-vivo
311 preparation of the Gerbil cochlea, but only under conditions that replicate a normal
312 endolymphatic potential and Ca^{2+} concentration (27). This nonlinearity disappears when no
313 endolymphatic potential is applied, which makes sense within the framework of our results: the
314 potential is then effectively very negative with respect to natural conditions—by 100 mV,
315 perhaps enforcing a similar state of weak gating force as we report here in frog upon application
316 of a potential that is negative enough (Fig. 1D, 2C and 4). Note that immersing the sensory

317 epithelium in artificial perilymph, as is routinely performed in the field, is also expected to lead
318 to weak gating forces but here as a result of a too high Ca^{2+} influx. In the cochlea, the Ca^{2+}
319 concentration in perilymph is indeed nearly two orders of magnitude higher than in endolymph.
320 Our results on frog saccular hair cells thus help putting ex-vivo measurements on mammalian
321 hair cells into prospective. In addition, our observations also imply that a spatial gradient in the
322 endolymphatic potential, as observed in vivo in the mammalian cochlea (28), might provide a
323 mechanism to tune the gating force and thus mechanosensitivity across hair cells.

324 In our experiments, control conditions approach natural conditions in the frog saccule: the
325 top and bottom compartments have ionic compositions that mimic those of endolymph and
326 perilymph, respectively, and there is no transepithelial potential. Also, our approach is based
327 on force measurements, which in contrast to standard electrophysiological approaches does not
328 disrupt the integrity of the hair cell or their internal ionic concentrations. Under these nearly
329 natural conditions, the gating force is strong, as a matter of fact strong enough to evoke negative
330 stiffness and promote spontaneous oscillations of the hair bundle (9). We applied
331 endolymphatic potentials within a range of ± 100 mV. While this range departs from natural
332 conditions, pushing the hair cells into uncharted territory disclosed gating-force control by the
333 endolymphatic potential and also indicated that the hair cell operates near an optimum of
334 mechanosensitivity under natural conditions.

335 It is worth noting that the potential difference between endolymph and the hair-cell interior
336 likely constitutes the relevant control parameter, not the endolymph potential per se. From this
337 perspective, modifying the endolymphatic potential may serve as a proxy for evaluating the
338 effects of varying the hair cell's transmembrane potential—at least insofar as
339 mechanosensitivity of the transduction channels is concerned. The efferent nervous system is
340 known to provide descending feedback from the brain to tune sensitivity of the auditory system
341 (29). Activation of the efferent system leads to hyperpolarization of the hair cell (30–32).
342 Assuming that hyperpolarization of the hair cell has similar effects on transduction channels'
343 operation as raising the endolymph potential to more positive values, our work opens the
344 possibility that efferent activation might affect the transduction channels' gating force and
345 gating swing.

346 **Effects of Ca^{2+} on hair-bundle mechanics**

347 Varying the endolymphatic potential afforded a means to reversibly and robustly control the
348 electric field in the membrane near the transduction channels and in turn the electromotive force

349 that controls the magnitude of transduction currents, including the Ca^{2+} influx into the hair cell.
350 Reducing the Ca^{2+} concentration near a hair bundle resulted in similar effects on gating
351 compliance and gating friction than applying negative endolymphatic potentials (Fig. 6). This
352 finding indicates that negative endolymphatic potentials modulated the gating force, at least in
353 part, by reducing the Ca^{2+} influx through the transduction channels. We cannot exclude,
354 however, that the endolymphatic potential also directly affected channel gating by mediating
355 an electric force on the transduction-channel protein complex. Depolarization of the hair cell
356 has been previously shown to evoke fast movements of the hair bundle, even with channels
357 blocked and thus with no change in the Ca^{2+} influx though the channels, which may be
358 indicative of a rearrangement of the channel protein complex (33, 34).

359 Calcium is also known to affect the channel activation time, the operating point of the
360 transducer and the kinetics of the active adaptation process that drives active hair-bundle
361 motility (4, 16, 18, 21–23, 35, 36). Moreover, there is some evidence that the extracellular
362 calcium concentration can modulate the stiffness of the hair bundle (23, 24, 37). In our
363 experiments, negative endolymphatic potentials produced effects on spontaneous hair-bundle
364 oscillations (fig. S3) that were qualitatively similar as those reported earlier in response to
365 depolarization of the hair cell (33) or to a decrease of the Ca^{2+} concentration in endolymph (18).
366 Conversely, positive endolymphatic potentials produced similar effects as hyperpolarization of
367 the hair cell or increasing the endolymphatic Ca^{2+} concentration.

368 Previous models had postulated stiffer gating springs at lower Ca^{2+} (18, 38), in apparent
369 contradiction with recent in-vitro measurements of PCDH15 elasticity (39). Our observations
370 (Figs. 2, 3 and 6) suggest instead that the effect of Ca^{2+} on gating-spring stiffness is small
371 compared to that on the gating swing, at least under our experimental conditions.

372 **Implications for the mechanism of channel gating**

373 As recognized earlier (9), we observed that the gating swing (Fig. 3) can be nearly one order of
374 magnitude larger than the expected diameter of the transduction channels' pore, which has been
375 estimated at about 1.2 nm (2). Hair cells thus appear to have implemented a mechanism to
376 magnify the conformational change associated to opening and closing of the transduction
377 channel's pore, a feature also relevant to other mechanosensitive channels (40). In hair cells,
378 the ion channels that mediate mechanoelectrical transduction are part of a molecular complex
379 that includes TMC1—the pore-forming subunit (41), TMIE, CIB2, LHFPL5 and the lower end
380 of the tip link, PCDH15 (42, 43). In addition, the complex may comprise two copies of each

381 protein, forming a dimeric assembly with an axis of twofold symmetry (44, 45) and comprising
382 a total of at least 10 proteins. Interactions between the multiple components of the transduction
383 apparatus might lead to a collective rearrangement upon opening of the channel's pore,
384 effectively producing a large gating swing. Alternatively, channel gating has been proposed to
385 elicit a membrane-mediated interaction between two channel complexes, each attached to one
386 strand of the PCDH15 dimer, leading to large movement within the membrane that magnifies
387 the apparent gating swing (46).

388 Whatever the molecular substrate for the gating swing, our work indicates that the
389 transepithelial potential and the extracellular calcium concentration can modulate the
390 magnitude of the movement associated to channel gating (Fig. 3). In addition, under conditions
391 for which the calcium influx through the channels becomes too low, we found that the gating
392 swing drops to undetectable levels. This observation suggests that the channel-protein complex
393 must be primed by enough intracellular calcium to elicit a large gating swing, perhaps via Ca^{2+}-
394 mediated conformational change in CIB2—the calcium- and integrin-binding protein (47, 48)
395 or by affecting the properties of the lipid membrane that houses the transduction channels (49).
396 Hysteresis upon a continuous back-and-forth variation of the endolymphatic potential (Fig. 4)
397 or of the extracellular concentration (Fig. 6), and the relatively short timescale of the transition
398 between states of strong and weak gating force (Fig. 5) provide further support for the bistability
399 of the channel-protein complex.

400 To cope with the physical requirements of hearing, hair cells have evolved the ability to
401 respond to sound stimuli that vary over timescales as short as a few tens of microseconds, detect
402 deflections of their hair bundle as small as one nanometer or less, and mediate sharp frequency
403 selectivity over three orders of magnitude of sound frequencies (50). These unique capabilities
404 rely on a transduction-channel protein complex with a highly intricate molecular composition
405 and architecture (43, 45). Inasmuch that the molecular underpinnings of mechanoelectrical
406 transduction by hair cells remains similar across species and organs, our force measurements
407 on hair bundles from frog saccular hair cells demonstrate that the effective conformational
408 change associated to channel gating—the gating swing—can be modulated over a broad range
409 by varying physiological control parameters. The modularity of the gating swing provides a
410 mechanism to tune passive and active mechanosensitivity of the hair cell while maintaining the
411 molecular composition of the transduction channels. Elucidating the molecular rearrangement

412 associated to channel gating and how it can be modulated remain major challenges for future
413 studies.
414

415 **METHODS**

416 **Experimental preparation**

417 All experimental procedures were approved by the Ethics committee on animal experimentation
418 of the Institut Curie; they complied with the European and French National Regulation for the
419 Protection of Vertebrate Animals used for Experimental and other Scientific Purposes
420 (Directive 2010/63; French Decree 2013–118). Details of the experimental preparation have
421 been published elsewhere (18, 23). Briefly, an excised preparation of the frog's saccule (Rivan
422 92 (51)) was glued with tissue-compatible surgical glue (Histoacryl, B. Braun) over a ~1 mm
423 hole in a plastic disk (fig. S2A). The preparation was then secured in a two-compartment
424 chamber, which exposed the apical and basal aspects of the sensory tissue to fluids with
425 different ionic compositions to mimic physiological conditions. The basal bodies of the hair
426 cells were bathed in artificial perilymph, a standard saline solution containing (in mM):
427 110 NaCl, 2 KCl, 1.5 $CaCl_2$, 3 D-glucose and 5 Hepes. Hair bundles instead projected into
428 artificial endolymph with (in mM): 2 NaCl, 118 KCl, 0.25 $CaCl_2$, 3 D-glucose, and 5 Hepes.
429 Each solution had a pH of ~ 7.3 and an osmotic strength of $\sim 225\ \mathrm{mmol \cdot kg^{-1}}$. To disconnect
430 the hair bundles from the overlying otolithic membrane, the apical surface of the preparation
431 was exposed for 20 min to endolymph supplemented with $67\ \mu\mathrm{g \cdot mL^{-1}}$ of the protease
432 subtilisin (type XXIV, Sigma). The otolithic membrane was then peeled off to obtain access to
433 individual hair bundles. Experiments were performed at a temperature of 20°C.

434 **Microscopic apparatus and mechanical stimulation**

435 The preparation was viewed through a $\times 60$ water-immersion objective of an upright
436 microscope (BX51WI, Olympus). The mechanical properties of single hair bundles were
437 characterized using published methods (8, 23). In short, the tip of a stimulus fiber was affixed
438 to the kinociliary bulb of an individual hair bundle and imaged at a magnification of $\times 944$ onto
439 a displacement monitor comprising a dual photodiode. Stimulus fibers were fabricated from
440 borosilicate capillaries (TW120-3, World Precision Instrument) and coated with a thin layer of
441 gold-palladium to enhance contrast (Hummer 6.1, Anatech ltd.). The fiber was secured by its
442 base to a stack-type piezoelectric actuator (PA-8/14, Piezosystem Jena) driven by a custom-
443 made power supply (Elbatech). Its stiffness, k_F, was estimated from the analysis of thermal
444 fluctuations at the fiber's tip.

445 In a first stimulation protocol, a series of step displacements, Δ, was applied to the fiber's
446 base. The standard protocol consisted in the application of 7 to 9 successive pairs of step
447 displacements in opposite directions with a magnitude growing with a constant increment,
448 within the range $20 - 40$ nm. The force, $F = k_F\ (\Delta - X)$, and the bundle's displacement, X,
449 were estimated $5\ -\ 9$ ms after the stimulus onset. This time was long enough for the open
450 probability of the transduction channels to have reached a new steady state and for the frictional
451 contribution to the applied force to have vanished, but short enough to limit the effect of
452 adaptation. The resulting force-displacement relation, $F(X)$, was fitted by the equation (5, 16):

$$F = KX - F_G/[1 + \exp(-(X - X_0)/\delta)] + F_\emptyset, \qquad (1)$$

453 from which we estimated the bundle's linear stiffness, K, the gating force, F_G, for the whole
454 hair bundle, and the set-point deflection, X_0. The parameter $F_\emptyset$ ensured that $F = 0$ at $X = 0$.
455 Because we did not use displacement-clamp feedback to stabilize positions of negative stiffness
456 (9), the characteristic displacement, δ, could not be exploited. In this protocol, both photodiode
457 and command signals were acquired and generated at a sampling rate of 2.5 kHz and the half-
458 power frequency of the lowpass filter was fixed at 1 kHz. A force-displacement relationship
459 was obtained by averaging 7 to 15 repetitions of the same stimulation protocol, which
460 collectively took 10 to 20 seconds.

461 In a second stimulation protocol, we applied a symmetric triangular waveform of motion to
462 the fiber's base, at a frequency of either 40 Hz or 100 Hz and with a peak-to-peak amplitude
463 within the range $600 - 1000$ nm. The force applied to the hair bundle was estimated using a
464 detailed description of the fiber's vibrational modes (8). This protocol resulted in force-
465 displacement cycles with counterclockwise circulation. The half-height at any position, X, in
466 the cycle provides an estimate of the average friction force $\phi(X) = [F^+(X) - F^-(X)]/2$
467 impeding the hair bundle motion at this position, where $F^\pm(X)$ represents the force in the
468 positive and negative half cycle of stimulation, respectively. The friction force displayed a
469 maximum, $\phi_{\mathrm{MAX}} = \phi(X_0)$, at a displacement that was identified earlier as the set-point
470 deflection X_0 in Equation 1 (8). The force-displacement cycle also displayed a point of
471 inversion symmetry of coordinates ($X_0,\ F_0 = [F^+(X_0) + F^-(X_0)]/2$). The shift, ΔX, between
472 the positions where the hair-bundle speed reached a maximal value, $|dX/dt| = V_{MAX}$, in the
473 positive and negative half cycle of stimulation provided an estimate of the activation time of
474 the transduction channels, $\tau = \Delta X/(2V_{MAX})$ (8). In this protocol, the force-displacement cycle

475 was averaged over ten periods of the triangular stimulus at 40 Hz or, when a fast assessment of
476 hair-bundle mechanics became necessary (as for the data shown in Fig. 5), over only two
477 periods of a 100-Hz stimulus. Both photodiode and command signals were acquired and
478 generated at sampling rate of 25 kHz. The half-power frequency of the filter was fixed at
479 12.5 kHz for the photodiode signals and 0.5 kHz for the command signals.

480 **Control of the transepithelial current and potential**

481 Using a current source (Linear Stimulator Isolator A395, World Precision Instruments)
482 connected to a pair of silver chloride electrodes (fig. S2A), we applied steps of transepithelial
483 current with a magnitude that was varied within a range of ± 10 μA. In some preparations, we
484 measured the transepithelial potential, $U(t)$, evoked by a step of transepithelial current, $I_{STEP} =$
485 1 μA (fig. S2B), using an additional pair of electrodes connected to the headstage of a
486 differential amplifier (voltage gain $\times$ 50; Model 3000, Systems Inc). The time course of the
487 transepithelial potential was well described by an exponential relation $U(t) = U_{MAX} \exp(-t/$
488 $\tau)$, with a characteristic timescale $\tau = 230 \pm 50$ μs (mean $\pm$ SD, n =13). Over an ensemble
489 of 13 saccules, we found a transepithelial resistance $R = U_{MAX}/I_{STEP} = 10 \pm 2$ kΩ and
490 capacitance $C = 23 \pm 4$ nF. Thus, over the range of transepithelial currents that we explored,
491 the potential into the artificial endolymph that bathed the hair bundles—the endolymphatic
492 potential— varied within a range of ± 100 mV with respect to the potential in the perilymphatic
493 compartment.

494 In other experiments, we applied successive ramps of descending and ascending
495 transepithelial currents at an absolute rate within the range of $0.5 - 0.9$ μA $\cdot$ s^{-1}. These rates
496 were low enough to ensure that the variation of the transepithelial current remained small during
497 the time required for probing hair-bundle mechanics, allowing these mechanical measurements
498 to remain quasistatic. The minimal current was maintained for $1 - 2.5$ s before the ascending
499 ramp started.

500 **Iontophoresis of a calcium chelator**

501 We used iontophoresis of a calcium chelator to decrease the extracellular calcium concentration
502 in the vicinity of individual hair bundles (13, 23). Coarse microelectrodes were fabricated from
503 borosilicate capillaries (TW120F-3, World Precision Instrument) with a pipette puller (P97,
504 Sutter Instrument); their resistance ranged from 0.8 to 1.5 MΩ when filled with 3-M KCl and
505 immersed in the same solution. The electrode's tip was positioned at ~3 μm from the hair
506 bundle.

In a first series of experiments, the electrodes were filled with 400-μM pentasodium triphosphate. Triphosphate allowed to decrease the calcium concentration while preserving the integrity of the tip links (23). A holding current of $+10$ nA was continuously applied to counteract the diffusive release of the calcium chelator from the electrode, to which we added either a step or a succession of descending and ascending ramps of iontophoretic current. The steps had a magnitude of varying between -80 nA and-60 nA, while the ramps reached a minimal value between -90 nA and-50 nA. The current varied at the same rate on the descending and ascending ramps, within a range $5 - 8\ \mathrm{nA} \cdot \mathrm{s}^{-1}$, and the minimal current was maintained for $1 - 2$ s before the ascending ramp started.

In a second series of experiments, we aimed at disrupting the tip links to evaluate their contribution to hair-bundle stiffness. In this case, the electrode was filled with EDTA at a concentration of 100 mM. We applied current steps of -100 nA on top of a resting current of $+10$ nA. In three cells, reducing the amplitude of the step to about -35 nA allowed to maintain the integrity of the tip links, adding data to those obtained with iontophoresis of triphosphate to evaluate the effects of reducing the calcium concentration on a force-displacement relation.

Signal generation and acquisition

All signals were generated and acquired under the control of a computer running a user interface programmed with the LabVIEW software (version 2011, National Instruments). Command signals were produced by a 16-bit interface card (PCI-6733, National Instruments). A second 16-bit interface card (PCI-6250, National Instruments) conducted signal acquisition. Sampling rates for signal generation and acquisition varied within the range $2.5 - 25$ kHz. All signals were conditioned with an eight-pole Bessel antialiasing filter (Model 3384, Krohn-Hite Corporation) at a lowpass cut-off frequency set at half the sampling frequency unless otherwise indicated.

Analysis of spontaneous hair-bundle oscillations

Details of the analysis of the spontaneous oscillations have been published elsewhere (20). Briefly, the displacement, $X(t)$, of an oscillating hair bundle was monitored over a duration of $10 - 30\ s$. The relation between its power spectrum, $C(f)$, and frequency, f, was first smoothed by a moving average with a frequency window of 1 Hz and then fitted by the sum of two Lorentzians

$$\tilde{C}(f) = \frac{A}{(f_0/2Q)^2 + (f - f_0)^2} + \frac{A}{(f_0/2Q)^2 + (f + f_0)^2}. \quad (2)$$

The fit provided values for the quality factor Q, the characteristic frequency f_0, and parameter A, which is related to the root-mean-square magnitude $X_{RMS} = \langle X(t) - \langle X(t)\rangle^2\rangle = \int_{-\infty}^{+\infty} \tilde{C}(f)df = \sqrt{4\pi AQ/f_0}$ of the movement. In cases where it was bimodal, the probability density of hair bundle positions was fitted by the sum of two Gaussian functions. The fractional area under the Gaussian that was centered at a positive position with respect to the mean bundle position provided a functional estimate of the open probability P_O^{SS} of transduction channels at steady state.

REFERENCE

1. A. J. Hudspeth, How the ear's works work. *Nature* **341**, 397–404 (1989).

2. R. Fettiplace, K. X. Kim, The physiology of mechanoelectrical transduction channels in hearing. *Physiol. Rev.* **94**, 951–86 (2014).

3. P. Martin, G. A. Manley, "Auditory processing by the cochlea" in *Principles of Neural Science*, McGraw-Hill Education / Medical; 6th edition, (2021), pp. 594–624.

4. D. P. Corey, A. J. Hudspeth, Kinetics of the receptor current in bullfrog saccular hair cells. *J. Neurosci.* **3**, 962-976. (1983).

5. V. S. Markin, A. J. Hudspeth, Gating-spring models of mechanoelectrical transduction by hair cells of the internal ear. *Annu. Rev. Biophys. Biomol. Struct.* **24**, 59–83 (1995).

6. J. Howard, A. J. Hudspeth, Compliance of the hair bundle associated with gating of mechanoelectrical transduction channels in the bullfrog's saccular hair cell. *Neuron* **1**, 189-199. (1988).

7. A. J. Ricci, A. C. Crawford, R. Fettiplace, Mechanisms of active hair bundle motion in auditory hair cells. *J. Neurosci.* **22**, 44–52 (2002).

8. V. Bormuth, J. Barral, J.-F. Joanny, F. Julicher, P. Martin, Transduction channels' gating can control friction on vibrating hair-cell bundles in the ear. *Proc. Natl. Acad. Sci. USA* **111**, 7185–7190 (2014).

9. P. Martin, A. D. Mehta, A. J. Hudspeth, Negative hair-bundle stiffness betrays a mechanism for mechanical amplification by the hair cell. *Proc. Natl. Acad. Sci. USA* **97**, 12026–12031 (2000).

10. I. J. Russell, M. Kossl, G. P. Richardson, Nonlinear mechanical responses of mouse cochlear hair bundles. *Proc. R. Soc. Lond. B* **250**, 217–27. (1992).

11. D. K. Chan, A. J. Hudspeth, Ca2+ current–driven nonlinear amplification by the mammalian cochlea in vitro. *Nat. Neurosci.* **8**, 149–155 (2005).

12. H. J. Kennedy, A. C. Crawford, R. Fettiplace, Force generation by mammalian hair bundles supports a role in cochlear amplification. *Nature* **433**, 880–883 (2005).

13. M. Tobin, A. Chaiyasitdhi, V. Michel, N. Michalski, P. Martin, Stiffness and tension gradients of the hair cell's tip-link complex in the mammalian cochlea. *eLife* **8**, e43473 (2019).

14. M. Beurg, E. T. Schwalbach, R. Fettiplace, LHFPL5 is a key element in force transmission from the tip link to the hair cell mechanotransducer channel. *Proc. Natl. Acad. Sci. USA* **121**, e2318270121 (2024).

15. P. Martin, A. J. Hudspeth, Active hair-bundle movements can amplify a hair cell's response to oscillatory mechanical stimuli. *Proc. Natl. Acad. Sci. USA* **96**, 14306–14311 (1999).

16. P. Martin, A. J. Hudspeth, Mechanical frequency tuning by sensory hair cells, the receptors and amplifiers of the inner ear. *Annu. Rev. Condens. Matter Phys.* **12**, 29–49 (2021).

17. P. Martin, A. J. Hudspeth, F. Julicher, Comparison of a hair bundle's spontaneous oscillations with its response to mechanical stimulation reveals the underlying active process. *Proc. Natl. Acad. Sci. USA* **98**, 14380–14385 (2001).

18. P. Martin, D. Bozovic, Y. Choe, A. J. Hudspeth, Spontaneous oscillation by hair bundles of the bullfrog's sacculus. *J. Neurosci.* **23**, 4533–4548 (2003).

19. D. Ramunno-Johnson, C. E. Strimbu, L. Fredrickson, K. Arisaka, D. Bozovic, Distribution of frequencies of spontaneous oscillations in hair cells of the bullfrog sacculus. *Biophys. J.* **96**, 1159–68 (2009).

20. J. Barral, F. Jülicher, P. Martin, Friction from transduction channels' gating affects spontaneous hair-bundle oscillations. *Biophys. J.* **114**, 425–436 (2018).

21. N. Hacohen, J. A. Assad, W. J. Smith, D. P. Corey, Regulation of tension on hair-cell transduction channels: displacement and calcium dependence. *J. Neurosci.* **9**, 3988-3997. (1989).

22. A. J. Ricci, Y. C. Wu, R. Fettiplace, The endogenous calcium buffer and the time course of transducer adaptation in auditory hair cells. *J. Neurosci.* **18**, 8261–77 (1998).

23. J.-Y. Tinevez, F. Jülicher, P. Martin, Unifying the various incarnations of active hair-bundle motility by the vertebrate hair cell. *Biophys. J.* **93**, 4053–4067 (2007).

24. R. E. Marquis, A. J. Hudspeth, Effects of extracellular Ca2+ concentration on hair-bundle stiffness and gating-spring integrity in hair cells. *Proc. Natl. Acad. Sci. USA* **94**, 11923–11928 (1997).

25. R. A. Jacobs, A. J. Hudspeth, Ultrastructural correlates of mechanoelectrical transduction in hair cells of the bullfrog's internal ear. *Cold Spring Harb. Symp. Quant. Biol.* **55**, 547–561 (1990).

26. C. Köppl, V. Wilms, I. J. Russell, H. G. Nothwang, Evolution of endolymph secretion and endolymphatic potential generation in the vertebrate inner ear. *Brain. Behav. Evol.* **92**, 1–31 (2018).

27. D. K. Chan, A. J. Hudspeth, Ca2+ current–driven nonlinear amplification by the mammalian cochlea in vitro. *Nat. Neurosci.* **8**, 149–155 (2005).

28. Y. Li, H. Liu, X. Zhao, D. Z. He, Endolymphatic Potential Measured From Developing and Adult Mouse Inner Ear. *Front. Cell. Neurosci.* **14**, 584928 (2020).

29. P. A. Fuchs, A. M. Lauer, Efferent Inhibition of the Cochlea. *Cold Spring Harb. Perspect. Med.* **9**, a033530 (2019).

30. M. Castellano-Muñoz, S. H. Israel, A. J. Hudspeth, Efferent Control of the Electrical and Mechanical Properties of Hair Cells in the Bullfrog's Sacculus. *PLoS ONE* **5**, e13777 (2010).

31. J. J. Art, R. Fettiplace, Efferent desensitization of auditory nerve fibre responses in the cochlea of the turtle Pseudemys scripta elegans. *J. Physiol.* **356**, 507–523 (1984).

32. C.-H. J. Lin, D. Bozovic, Effects of Efferent Activity on Hair Bundle Mechanics. *J. Neurosci.* **40**, 2390–2402 (2020).

33. S. W. Meenderink, P. M. Quinones, D. Bozovic, Voltage-mediated control of spontaneous bundle oscillations in saccular hair cells. *J. Neurosci.* **35**, 14457–66 (2015).

34. E. L. Cheung, D. P. Corey, Ca2+ changes the force sensitivity of the hair-cell transduction channel. *Biophys J* **90**, 124–39 (2006).

35. Y. C. Wu, A. J. Ricci, R. Fettiplace, Two components of transducer adaptation in auditory hair cells. *J Neurophysiol* **82**, 2171–81 (1999).

36. A. J. Ricci, H. J. Kennedy, A. C. Crawford, R. Fettiplace, The transduction channel filter in auditory hair cells. *J. Neurosci.* **25**, 7831–9 (2005).

37. M. Beurg, J.-H. Nam, A. Crawford, R. Fettiplace, The actions of calcium on hair bundle mechanics in mammalian cochlear hair cells. *Biophys. J.* **94**, 2639–2653 (2008).

38. Y. Roongthumskul, L. Fredrickson-Hemsing, A. Kao, D. Bozovic, Multiple-timescale dynamics underlying spontaneous oscillations of saccular hair bundles. *Biophys. J.* **101**, 603–610 (2011).

39. Villasante, C. M., Deng, X., Cohen, J. E., Hudspeth, A.J., Nanomechanics of wild-type and mutant dimers of the inner-ear tip-link protein protocadherin 15. *Proc. Natl. Acad. Sci. USA* **121**, e2404829121 (2024).

40. Y. R. Guo, R. MacKinnon, Structure-based membrane dome mechanism for Piezo mechanosensitivity. *eLife* **6**, e33660 (2017).

41. B. Pan, *et al.*, TMC1 forms the pore of mechanosensory transduction channels in vertebrate inner ear hair cells. *Neuron* **99**, 736-753.e6 (2018).

42. W. Zheng, J. R. Holt, The mechanosensory transduction machinery in inner ear hair cells. *Annu. Rev. Biophys.* **50**, 31–51 (2021).

43. X. Qiu, U. Müller, Sensing sound: Cellular specializations and molecular force sensors. *Neuron* **110**, 3667–3687 (2022).

44. J. Ge, *et al.*, Structure of mouse protocadherin 15 of the stereocilia tip link in complex with LHFPL5. *eLife* **7**, e38770 (2018).

45. H. Jeong, *et al.*, Structures of the TMC-1 complex illuminate mechanosensory transduction. *Nature* **610**, 796–803 (2022).

46. F. Gianoli, T. Risler, A. S. Kozlov, Lipid bilayer mediates ion-channel cooperativity in a model of hair-cell mechanotransduction. *Proc. Natl. Acad. Sci. USA* **114**, E11010–E11019 (2017).

47. R. Vallone, G. Dal Cortivo, M. D'Onofrio, D. Dell'Orco, Preferential binding of Mg2+ over Ca2+ to CIB2 triggers an allosteric switch impaired in Usher syndrome type 1J. *Front. Mol. Neurosci.* **11**, 274 (2018).

48. S. Wu, *et al.*, Mechano-electrical transduction components TMC1-CIB2 undergo a Ca2+-induced conformational change linked to hearing loss. *Dev. Cell* S1534580725000048 (2025). https://doi.org/10.1016/j.devcel.2025.01.004.

49. S. S. George, C. R. Steele, A. J. Ricci, Rat Auditory Inner Hair Cell Mechanotransduction and Stereociliary Membrane Diffusivity Are Similarly Modulated by Calcium. *iScience* **23**, 101773 (2020).

50. A. J. Hudspeth, P. Martin, The Critical Thing about the Ear's Sensory Hair Cells. *J. Neurosci.* **44**, e1583242024 (2024).

51. A. Neveu, Suitability of European green frogs for intensive culture: Comparison between different phenotypes of the esculenta hybridogenetic complex. *Aquaculture* **295**, 30–37 (2009).

Acknowledgements

Funding:

Fondation pour l'Audition grant FPA RD 2020-7 (PM)

Labex Cell(n)Scale grant ANR-11-LABX-0038 (PM)

Labex Cell(n)Scale grant ANR-10-IDEX-001-02 (PM)

Université Paris Sciences et Lettres and doctoral school "Physique en Île-de-France" grant (AJ)

Author contributions:

Competing interest:

The authors declare that they have no conflict of interest.

Data and materials availability: All data needed to evaluate the conclusions in the paper are present in the paper and/or the Supplementary Materials. Datasets for all the figures in the Main Text and Supplementary materials can be found on Zenodo (https://doi.org/10.5281/zenodo.14452874). Additional data related to this paper may be requested from the authors.

MAIN-FIGURE LEGENDS

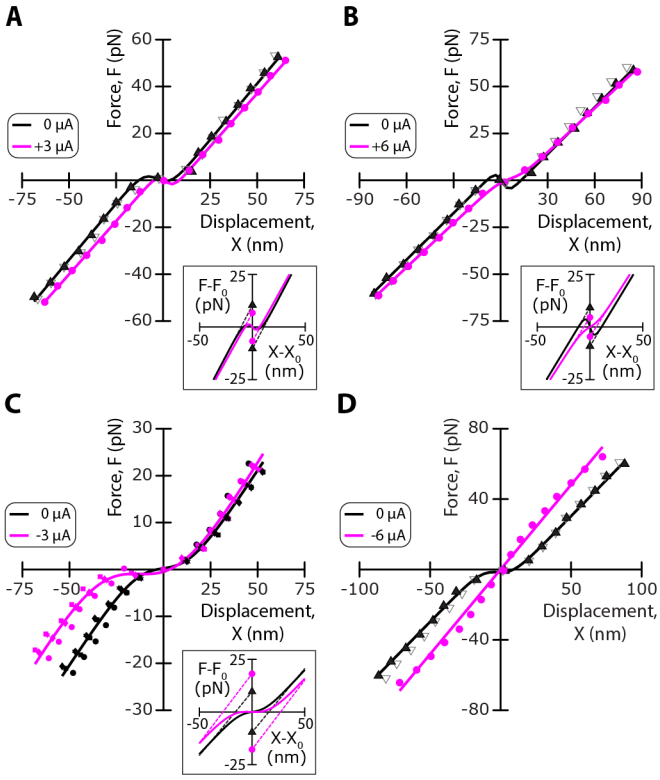

Fig. 1 : Representative examples of mechanical changes evoked by a transepithelial current. (A-D) Force-displacement relations, $F(X)$, for four different hair bundles under control conditions ($I = 0$ μA; black) and in the presence of a transepithelial current (magenta) of amplitude $I = +3$ μA (A), $I = +6$ μA (B), $I = -3$ μA (C) and $I = -6$ μA (D). Each relation was fitted by Equation 1 (solid lines; parameter values in table S1). Insets: the fitted curves are replotted with respect to the origin $(X_0, F(X_0))$, where X_0 is the set-point deflection. Under each condition, the hair bundle's gating force, F_G, was given by the vertical distance between the two symbols in the inset ($I = 0$: triangles; $I \neq 0$: disks). In (A), (B) and (D), the open black symbols correspond to a measurement after restoring control conditions to assess reversibility; in (C), the experiment was repeated 4 times.

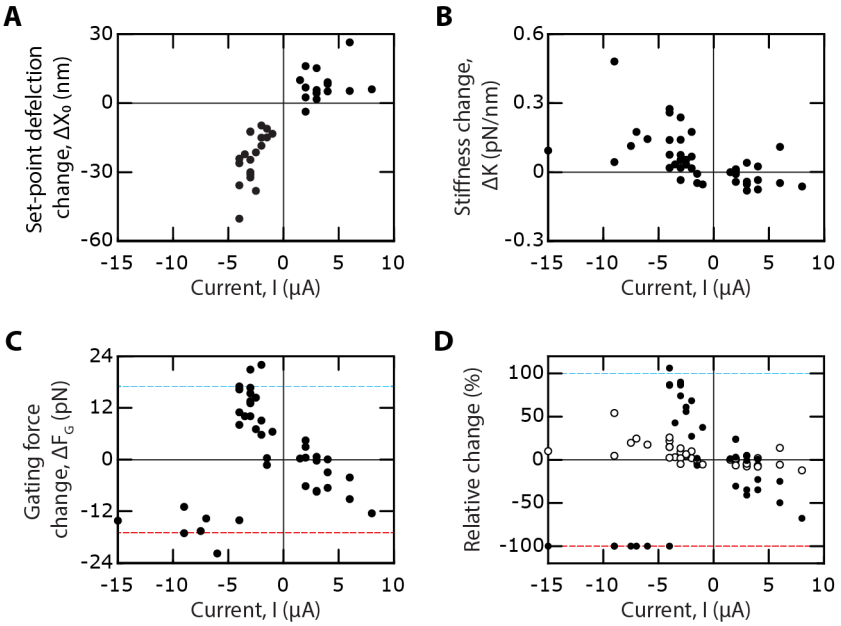

Fig. 2 : Changes in set-point deflection, stiffness and gating force upon application of a transepithelial current. **(A)** The change, ΔX_0, of the set-point deflection showed a strong positive correlation to the transepithelial current, I (Pearson correlation r $= 0.87$; p-value: $4 \cdot 10^{-11}$; $n = 34$). **(B)** The change, ΔK, of the linear stiffness was negatively correlated to the current, but only weakly (Pearson correlation r $= -0.57$; p-value: 10^{-4}; $n = 41$). **(C)** For I > -4 μA, the change, ΔF_G, of the bundle's gating force showed a strong negative correlation to the current (Pearson correlation r $= -0.86$; p-value: $8 \cdot 10^{-11}$; $n = 34$). **(D)** Relative change of the hair-bundle's gating force, $\Delta F_G / F_G(0)$ (solid disks) and linear stiffness, $\Delta K / K(0)$ (open disks) as a function of the transepithelial current, I. Under control conditions ($I = 0$), the gating force was $F_G = 17 \pm 4$ pN (mean $\pm$ SD, $n = 29$). In (C) and (D), the red and blue dashed lines mark, respectively, a reduction and an increase of the gating force by 100% with respect to the mean value under control conditions. For $I < -5$ μA, all the force displacement relations were linear: the gating force had dropped to undetectable levels and the set-point deflection could no longer be measured from the mechanics.

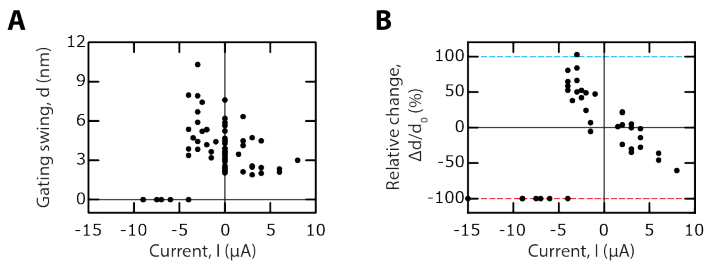

Fig. 3: Electrical control of the gating swing. The gating swing, d, **(A)** and its relative change, $\Delta d/d_0$, **(B)** are shown as a function of the transepithelial current, I, where $\Delta d = d(I) - d(I = 0)$ and $d_0 = d(I = 0)$. For $I \geq -5$ μA, the relative change displayed a strong negative correlation to the current (Pearson correlation $r = -0.86$; p-value: $1 \cdot 10^{-10}$). Same dataset as that used in Fig. 2. After each measurement of a bundle's force-displacement relation, the gating swing was estimated as $d = \gamma F_G/(K - K_{SP})$, where F_G and K are respectively the gating force and linear stiffness resulting from a fit of the force-displacement relation with Equation 1 and K_{SP} is the mean stiffness measured over an ensemble of hair bundles after disruption of their tip links. The projection factor $\gamma = 0.14$ was used to estimate the gating swing along the oblique axis of the tip link.

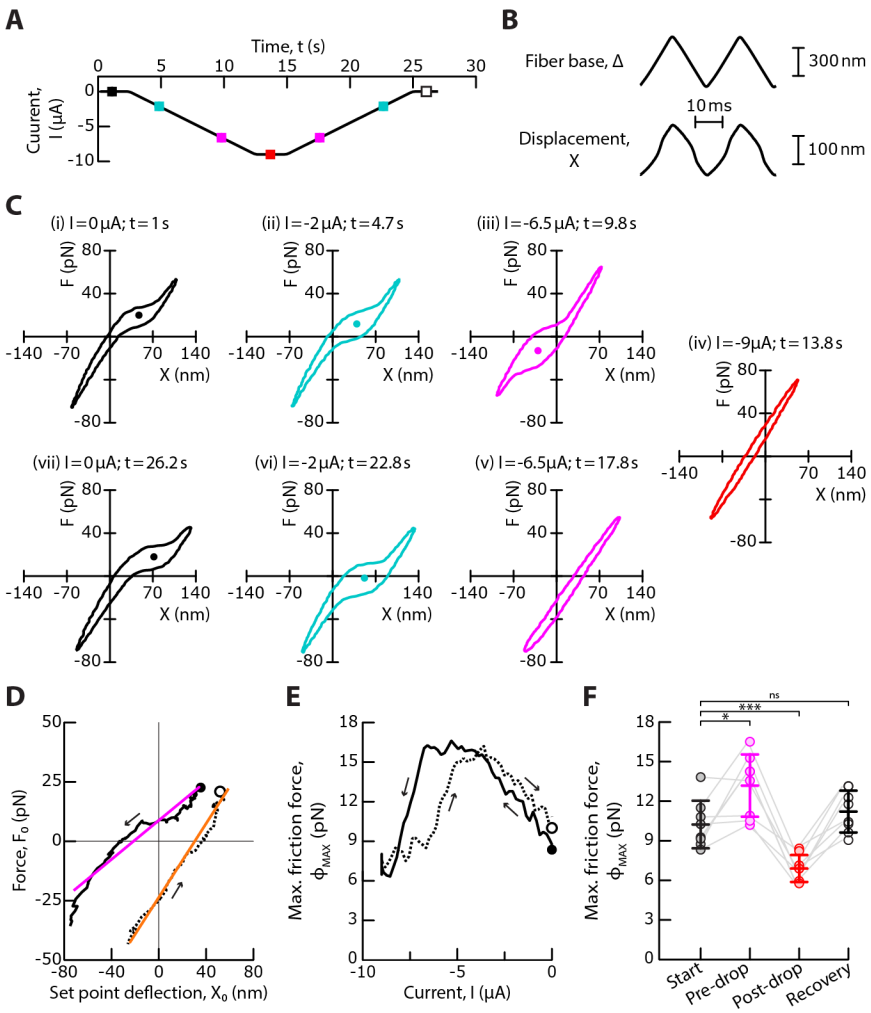

Fig. 4 : **Transition between states of strong and weak gating force.** **(A)** A descending ramp of a negative transepithelial current was followed by an ascending ramp of current at the same absolute rate of 0.9 $\mu A \cdot s^{-1}$. The colored square symbols indicate the time points of the analysis shown in (C). **(B)** The hair bundle was continuously moved back and forth (bottom) by imposing a periodic triangular movement to the stimulus fiber's base, here with a peak-to-peak amplitude of 600 nm and at a frequency of 40 Hz (top). The movements were averaged over 10 stimulus cycles. **(C)** Force-displacement cycles for the values of the transepithelial current and at times indicated at the top of each sub-panel (see colored square symbols in (A)). **(D)** Trajectory of the point of inversion symmetry (X_0, F_0) in a force-displacement cycle, marked by disks in (C). Linear fits to these trajectories: $F_0 = 0.41 \cdot X_0 + 9$ ($R^2 = 0.92$) (magenta) and $F_0 = 0.78 \cdot X_0 + 24$ ($R^2 = 0.98$) (orange), respectively. **(E)** Maximal friction force, ϕ_{MAX}, as a function of the transepithelial current, I. **(F)** For all the 8 different hair bundles that followed the same protocol, the maximal friction force, ϕ_{MAX}, first increased as the

transepithelial current decreased, before dropping to a low value as the hair bundle transitioned from a state of strong gating force to a state of weak gating force at more negative values of the current than a threshold $I = I_{DROP} = -3.7 \pm 1$ μA (mean $\pm$ SD, $n = 8$). Colored disks mark, for each hair-bundle, the value of ϕ_{MAX} at the start of the experiment ($I = 0$, black), before ($I = I_{DROP} + 1$ μA, magenta) and after ($I = -9$ μA, red) the drop of ϕ_{MAX}, and at the end of the experiment ($I = 0$ μA, white). Error bars: mean $\pm$ SD. Statistical significance was assessed using a paired t-test with p-values from left to right: $2 \cdot 10^{-2}$, $8 \cdot 10^{-4}$, 10^{-1}. ns > 0.05, * p-value ≤ 0.05, *** p-value ≤ 0.001. In (D-E), black solid and dashed lines correspond to the descending and ascending ramps of transepithelial currents, respectively. Arrows indicate the direction of circulation along the curve from start (black disk) to finish (white disk).

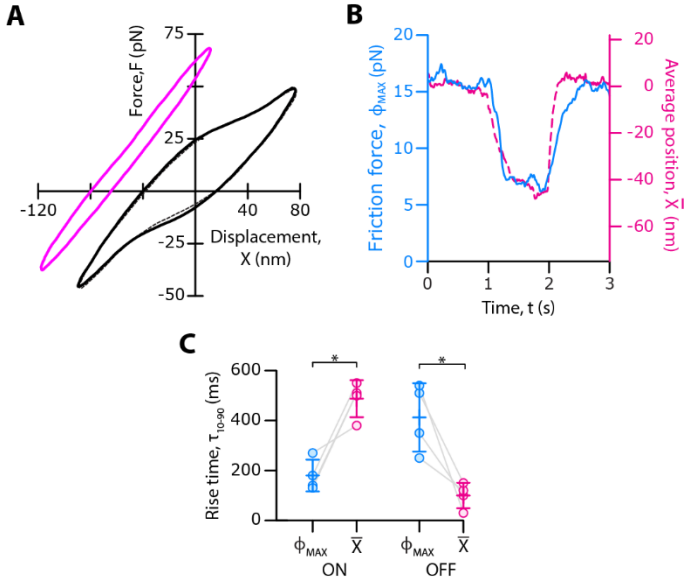

Fig. 5 : Transition kinetics between states of strong and weak gating force. **(A)** Force-displacement cycle here averaged over 50 cycles of stimulation, under control conditions ($I = 0$; black solid line), 400 ms after the onset of a step of transepithelial current ($I = -8$ µA; magenta) and 600 ms after termination of the current step ($I = 0$; black dashed line). **(B)** Time course of the maximal friction force, ϕ_{MAX}, (blue line) and of the average displacement, $\bar{X}$, (dashed magenta line) in a force-displacement cycle. The current step started at $t = 1$ s and ended at $t = 2$ s. **(C)** For all the 4 different hair bundles that followed the same protocol, time, τ_{10-90}, required for the maximal friction force, ϕ_{MAX} (blue disks), and the average displacement, $\bar{X}$ (magenta disks), to transition from 10% to 90% of the total change after the onset (ON) and the termination (OFF) of a step of transepithelial current ($I = -8$ µA). Error bars indicate the mean $\pm$ SD. Statistical significance was assessed using a paired t-test with p-values from left to right: $2 \cdot 10^{-2}$, $3 \cdot 10^{-2}$; * p-value ≤ 0.05. The base of the stimulus fiber followed a periodic triangular waveform of motion, with a peak-to-peak amplitude of 600 nm and at a frequency of 100 Hz. For the data shown in (B) and (C), the force-displacement cycles were averaged over only two cycles of stimulation.

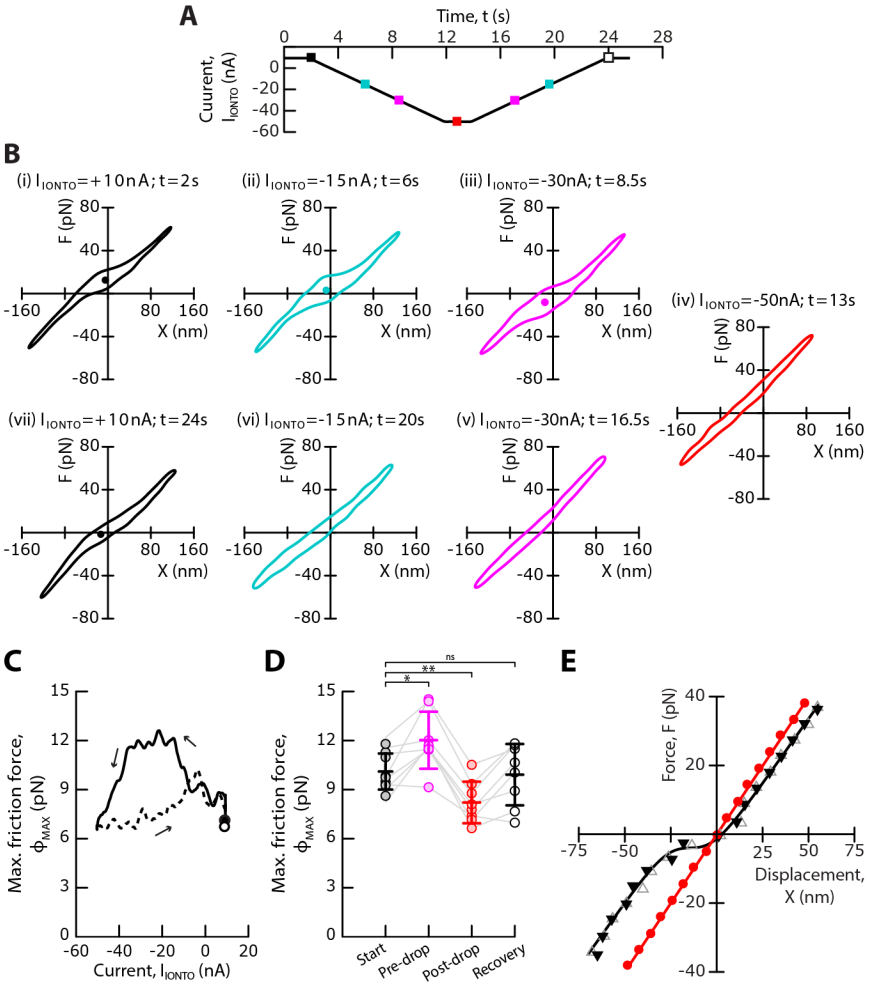

Fig. 6 : Replicating the effects of negative endolymphatic potentials with iontophoresis of a Ca^{2+} chelator. **(A)** We used iontophoresis of a calcium chelator to decrease the extracellular Ca^{2+} concentration in the vicinity of a hair bundle. A descending ramp of a negative iontophoretic current, I_{IONTO}, which was carried in part by a Ca^{2+}chelator, was followed by an ascending ramp of current at the same absolute rate of $6.6\ \mathrm{nA} \cdot \mathrm{s}^{-1}$. The colored square symbols indicate the time points of the analysis shown in (B). **(B)** Each sub-panel shows the bundle's force-displacement cycle in response to a triangular mechanical stimulus for the value of the iontophoretic current, I_{IONTO}, and at the time, t, indicated at the top. **(C)** Maximal friction force, ϕ_{MAX}, as a function of the iontophoretic current, I_{IONTO}, which varied in time from start (black disk) to finish (white disk). Arrows indicate the direction of circulation along the curve. Solid and dashed lines correspond to the descending and ascending ramps of iontophoretic currents, respectively. **(D)** For all the 8 different hair bundles that followed the same protocol, the maximal friction force, ϕ_{MAX}, first increased as the extracellular Ca^{2+} concentration

decreased, before dropping to a low value as the hair bundle transitioned from a state of strong gating force to a state of weak gating force at more negative values of the iontophoretic current than a threshold $I_{IONTO} = I_{DROP} = -40 \pm 10$ nA (mean $\pm$ SD, $n = 8$). Colored disks mark, for each hair-bundle, the value of ϕ_{MAX} at the start of the experiment ($I_{IONTO} = +10$ nA, black), before ($I_{IONTO} = I_{DROP} + 5$ nA, magenta) and after ($I_{IONTO} = -50$ nA, red) the drop of ϕ_{MAX}, and at the end of the experiment ($I_{IONTO} = +10$ nA, white). Error bars: mean $\pm$ SD. Statistical significance was assessed using a paired t-test with p-values from left to right: $1.5 \cdot 10^{-2}$, $5 \cdot 10^{-3}$, $6 \cdot 10^{-1}$; ns > 0.05; * p-value ≤ 0.05, ** p-value ≤ 0.01. (E) The force-displacement relation of a different hair bundle displays a region of gating compliance under control conditions (black triangles) but was linear in the presence of a steady iontophoretic current of -60 nA (red circle). This effect was reversible (grey triangles). Each force-displacement relation was fitted by Equation 1 (solid lines; parameter values in table S1). In (B-D), a periodic triangular waveform of motion was applied to the base of the stimulus fiber, with a peak-to-peak amplitude of 600 nm and at a frequency of 40 Hz. In (E), force-displacement relations were instead measured in response to step displacements at the base of the stimulus fiber (see Methods).

Supplementary Materials for

Electrical control of the transduction channels' gating force in sensory hair cells

Achille Joliot[1,2] , Laure Stickel[1,2] and Pascal Martin[1,2,*]

[1] Physique des Cellules et Cancer, Institut Curie, PSL Research University, CNRS UMR168, F-75248 Paris, France.

[2] Sorbonne Université, F-75252 Paris, France.

[*] Correspondence: pascal.martin@curie.fr

The supplementary materials include:

Table S1

Figures S1 to S4

Legends for Movies S1 to S3

Other supporting materials for this manuscript include the following:

Movies S1 to S3

822 **Supplementary Table**

823 **Table S1** Parameter values for fits of force-displacement relations with Equation 1.

Variable	Definition	Fig. 1A		Fig. 1B		Fig. 1C		Fig. 1D		Fig. 5E	
I (μA)	Transepithelial current	0	+3	0	+6	0	−3	0	−6	n/a	n/a
I_{IONTO} (nA)	Iontophoretic current,	n/a	n/a	n/a	n/a	n/a	n/a	n/a	n/a	+10	−60
X_0 (nm)	Set-point deflection	−3	1	1	+6	−0.2	−12.7	−2	n/a	−14	n/a
K ($\mathrm{pN \cdot nm^{-1}}$)	Stiffness	0.96	0.91	0.83	0.78	0.6	0.66	0.82	0.96	0.75	0.80
F_G (pN)	Gating force	21	13	18	9	19	36	22	n/a	22	n/a
δ (nm)	Characteristic length	4	2	2	5	8.9	13	6	n/a	7	n/a
$F_\emptyset$ (pN)	Force constant	14	5	7	0.6	10	25	11	n/a	18	n/a
R^2	Coefficient of determination	0.999	0.994	0.986	0.986	0.986	0.986	0.986	0.986	0.979	0.993

824

825

Supplementary Figures

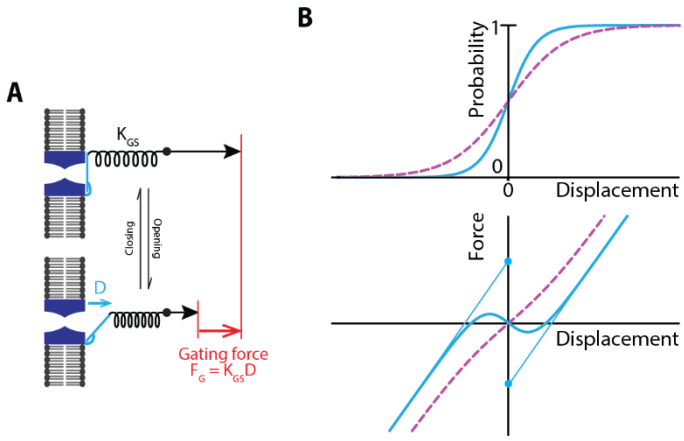

Fig. S1 : Gating-spring model of mechanoelectrical transduction. **(A)** The concept of gating force. When the transduction channels switch between their open and closed state, tension in the gating springs is reduced (black arrows); this mechanical correlate of channel gating is called the gating force, $F_G = K_{GS} \cdot D$ (red arrow), where K_{GS} is the combined stiffness of all the gating springs operating in parallel in the hair bundle and D is the gating swing of each channel. **(B)** Electrical and mechanical responses to hair-bundle displacement. Top: sigmoidal relationship of channel open probability to displacement in the case of weak (dashed magenta line) and strong (solid blue line) gating force. The larger the gating force, the steeper the sigmoid and the more sensitive the hair cell is to displacement of its hair bundle. Bottom: The force–displacement relationship displays a shallow nonlinearity when sensitivity is low (dashed magenta curve) and a strong nonlinearity when sensitivity is high (smooth blue curve). The gating force is given by the vertical shift between the two linear limbs of the force-displacement relation; it is here shown in the case of high sensitivity as the distance between the two disks.

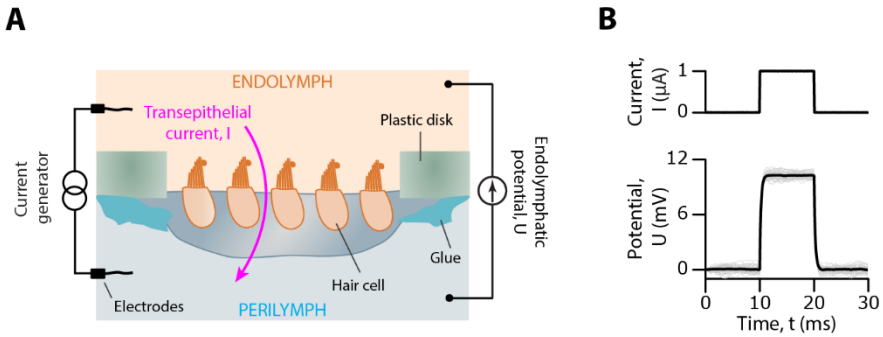

Fig. S2 : Two-compartment ex-vivo preparation of the frog saccule. **(A)** Schematic of the setup. The tissue was glued over a 1-mm hole in a plastic disk. Its apical and basal aspects were bathed in artificial endolymph and perilymph, respectively. A transepithelial current, I, was produced by a pair of silver chloride electrodes connected to a current generator, resulting in an endolymphatic potential, U, with respect to the potential in perilymph. The sign convention is such that positive currents lead to a positive value of the endolymphatic potential. **(B)** A +1-µA step of transepithelial current (top) evoked an endolymphatic potential $U \simeq +10$ mV at steady state (bottom, grey), corresponding to a transepithelial resistance of 10 kΩ. An exponential fit (black line), $U(t) = A\exp(-t/\tau)$, to the response yielded the amplitude $A =$ 10.2 mV and the characteristic time $\tau = 210$ µs.

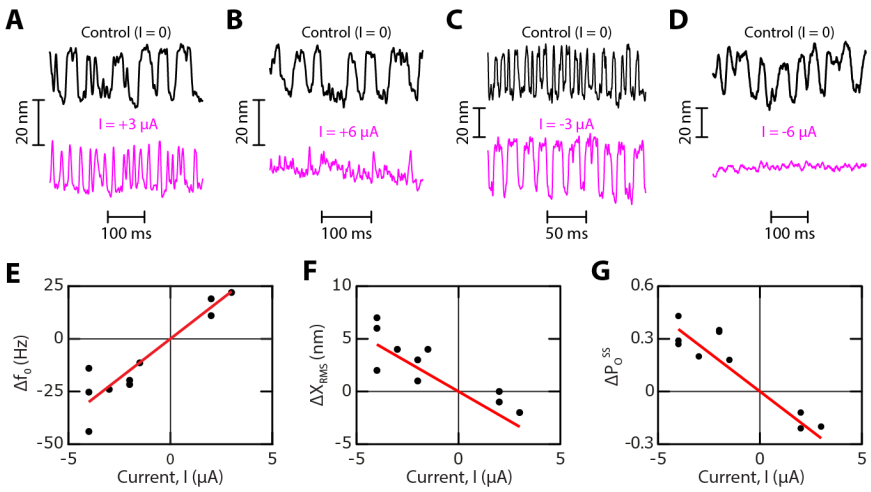

Fig. S3 : Effects of a transepithelial current on spontaneous hair-bundle oscillations. Under control conditions ($I = 0$), over an ensemble of $n = 10$ oscillatory hair bundles, the oscillations had a characteristic frequency $f_0 = 22 \pm 14$ Hz, a root-mean-squared (RMS) amplitude $X_{RMS} = 13 \pm 4$ nm and their bimodal position histograms were associated with a steady-state open probability for the transduction channels $P_O^{SS} = 0.4 \pm 0.1$, thus close to $1/2$. These characteristics are remarkably similar to those reported earlier with hair cells from a different frog species (18, 20). **(A-D)** Representative examples of spontaneous hair-bundle oscillations under control conditions ($I = 0$; top) and in the presence of a transepithelial current (bottom) $I = +3$ μA (A), $I = +6$ μA (B), $I = -3$ μA (C), and $I = -6$ μA (D). **(E)** The change, Δf_0, of the oscillation frequency displayed a strong positive correlation to the transepithelial current (Pearson correlation $r = +0.9$; p-value $= 10^{-4}$; $n = 10$). **(F)** The change, ΔX_{RMS}, of the RMS amplitude of spontaneous oscillations displayed a strong negative correlation to the transepithelial current (Pearson correlation $r = -0.9$; p-value $= 1 \cdot 10^{-3}$; $n = 10$). **(G)** The change, ΔP_O^{SS}, of the open probability at steady state displayed a strong negative correlation to the transepithelial current (Pearson correlation $\mathrm{r} = -0.9$, p-value $= 1 \cdot 10^{-4}$, $n = 10$). In (A), the transepithelial current evoked an increase of the oscillation frequency from 17 Hz to 39 Hz, a decrease of the RMS amplitude of oscillation from 7 nm to 5 nm and a decrease of the steady-state open probability from 0.5 to 0.3. Conversely in (B), the frequency of oscillation decreased from 49 Hz to 25 Hz, the RMS amplitude of oscillation increased from 11 nm to 15 nm and the steady-state open probability increased from 0.4 to 0.6. In the presence of a large positive current ($I = +6$ μA; panel B), the hair bundle only produced irregular spiky movements in the positive direction: the transduction channels were closed most of the time and evinced brief openings. Instead, a large negative current ($I = -6$ μA; panel D) completely abolished

spontaneous oscillations. Red lines in (E-G) correspond to proportional fits of respective slopes $7\ \mathrm{Hz} \cdot \mu\mathrm{A}^{-1}$ ($R^2 = 0.86$; panel E), $-1.1\ \mathrm{nm} \cdot \mu\mathrm{A}^{-1}$ ($R^2 = 0.6$; panel F), and $-0.08\ \mu\mathrm{A}^{-1}$ ($R^2 = 0.83$; panel G).

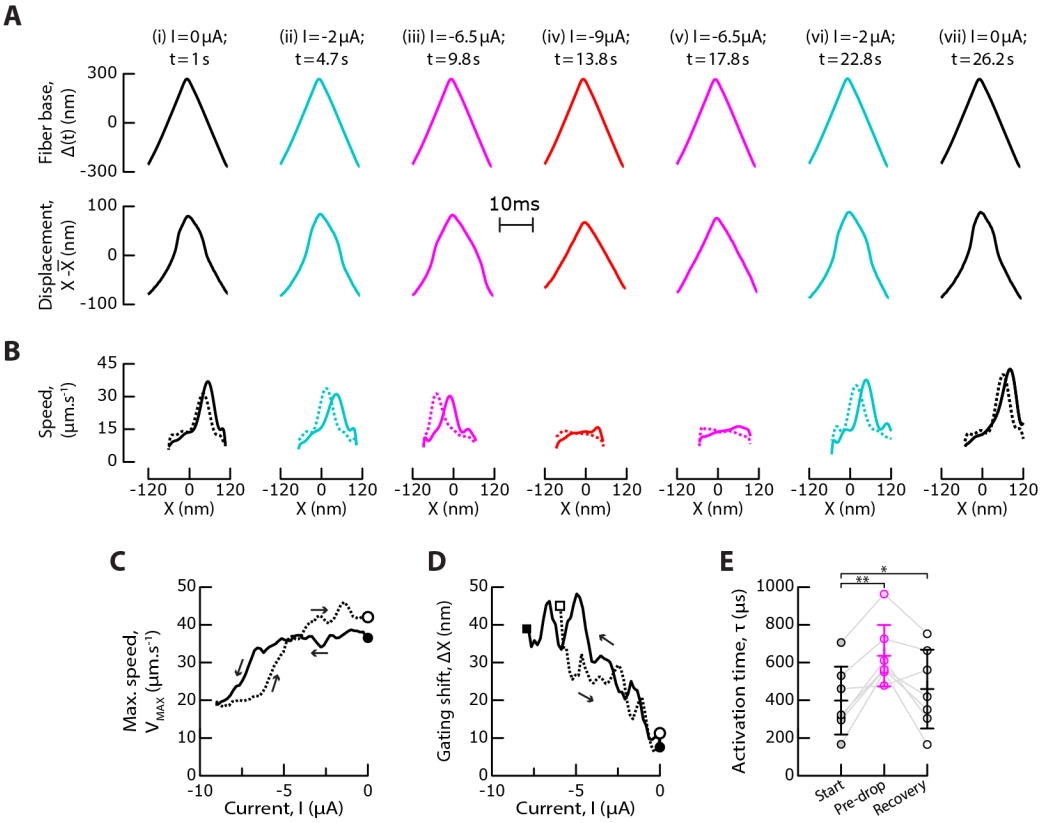

Fig. S4 : Effect of a transepithelial current on the channel-activation time. Same data as in Fig. 4A-E, to which this figure is associated. The time course of successive ramps of descending and ascending transepithelial current can be found in Fig. 4A. **(A)** Fiber-base displacement, Δ (*top*), and hair-bundle displacement, X (*bottom*), as a function of time for one stimulus cycle at time points and values of the transepithelial current indicated at the top of each time trace. **(B)** Hair-bundle speed, $|dX/dt|$, on the positive (*solid line*) and negative (*dashed line*) half cycles of mechanical stimulation as a function of displacement, X. The distance between the two peaks, ΔX, defines the gating shift. **(C-D)** Maximum speed, V_{MAX} (C), and gating shift, ΔX (D), as a function of the transepithelial current, I, which varied in time from start (black disk) to finish (white disk). Arrows indicate the direction of circulation along the curve. Solid and dashed lines correspond to the descending and ascending ramps of transepithelial currents, respectively. In panel (D), a black square indicates the current at which the signatures of gating compliance and gating friction vanished on the descending ramp; bellow this current, the gating shift is no longer defined. Conversely, a white square indicates recovery of the signatures of gating compliance and gating friction on the ascending ramp. **(E)** For the same ensemble of hair bundles as in Fig. 4, the distributions of the estimated activation time of the transduction channel, $\tau = \Delta X/(2\, V_{MAX})$, are shown at the start of the experiment ($I = 0$, black), before the

drop of the maximal friction force (magenta, see Fig. 4F), and at the end of the experiment ($I = 0$, white). Error bars: mean $\pm$ SD. Statistical significance was assessed using a paired t-test with, from p-values from left to right: $0.0014, 0.021$ *p-value ≤ 0.05, **p-value ≤ 0.01.

Legends for supplementary movies

Movie S1 (separate file): Transition between states of strong and weak gating force. Movie associated to Fig. 3A-E. The force-displacement cycle in response to triangular mechanical stimulation of the hair bundle (top) is shown over time as the transepithelial current follows successive descending and ascending ramps (bottom). The friction force, $\phi(X)$, at each displacement X of the hair bundle is color coded as indicated on the right; it is given by the half-height of the force-displacement cycle. To obtain smooth videos, the force-displacement cycles were here averaged over 15 cycles, instead of 10 cycles in the data shown in Fig. 3.

Movie S2 (separate file): Kinetics of the transition between states of strong and weak gating force. Movie associated to Fig. 4A-B. The force-displacement cycle in response to triangular mechanical stimulation of the hair bundle (top) is shown over time before, during and after application of a negative step of transepithelial current (bottom). The friction force, $\phi(X)$, at each displacement X of the hair bundle is color coded as indicated on the right; it is given by the half-height of the force-displacement cycle. The force-displacement cycles were here averaged over 5 cycles.

Movie S3 Transition between states of strong and weak gating force upon a decrease of extracellular calcium concentration. Movie associated to Fig. 5A-D. The force-displacement cycle in response to triangular mechanical stimulation of the hair bundle (top) is shown over time as an iontophoretic current trough a pipette containing a calcium chelator and positioned near a hair bundle follows successive descending and ascending ramps (bottom). The friction force, $\phi(X)$, at each displacement X of the hair bundle is color coded as indicated on the right; it is given by the half-height of the force-displacement cycle. To obtain smooth videos, the force-displacement cycles were here averaged over 15 cycles, instead of 10 cycles for the data shown in Fig. 5.